PHYSICAL REVIEW B **99**, 184111 (2019)

Predicting three-dimensional icosahedron-based boron B_{60}

Xin-Ling He,[1,*] Xi Shao,[2,*] Tong Chen,[3] Yu-Ke Tai,[1] Xiao-Ji Weng,[1] Qun Chen,[3] Xiao Dong,[1,†]
Guoying Gao,[2] Jian Sun,[3] Xiang-Feng Zhou,[1,2,‡] Yongjun Tian,[2] and Hui-Tian Wang[1,3]
[1]*Key Laboratory of Weak-Light Nonlinear Photonics and School of Physics, Nankai University, Tianjin 300071, China*
[2]*Center for High Pressure Science, State Key Laboratory of Metastable Materials Science and Technology,*
School of Science, Yanshan University, Qinhuangdao 066004, China
[3]*National Laboratory of Solid State Microstructures, School of Physics and Collaborative Innovation*
Center of Advanced Microstructures, Nanjing University, Nanjing 210093, China

(Received 31 December 2018; revised manuscript received 6 May 2019; published 23 May 2019)

The icosahedron-based bulk boron structures have extremely chemical and structural complexity, and are usually semiconductors at ambient conditions. Here we predict bulk boron phases with a 60-atom orthorhombic unit cell from an *ab initio* evolutionary structure search, termed as B_{60}. The metastable structures can be either a conductor or a semimetal depending on their interstitial atomic positions. In particular, an orthorhombic structure with *Pnma* symmetry (*Pnma*-B_{60}), consisting of B_{12} icosahedra and twisted interstitial two-atom wide boron ribbons, is identified to be a topological node-line semimetal with potential superior electronic transport. The band structure and simulated electron-diffraction pattern of *Pnma*-B_{60} are in satisfactory agreement with the experimental data, suggesting that it may exist in the form of nanomaterials.

DOI: 10.1103/PhysRevB.99.184111

I. INTRODUCTION

Boron is a promising element with a huge range of applications from nuclear reactors to thermoelectric, superhard, and high-energy materials. It forms various complex structures owing to the electron-deficient bonding nature, which results in a rather confusing phase diagram [1–9]. As carbon's neighbor in the periodic table, boron's valence electrons are too localized to form a simple covalent structure, but are able to form nanostructures just as carbon, i.e., clusters, fullerenes, nanotubes, nanowires, nanoribbons, nanobelts, and nanosheets associated with low density, high strength, and high melting point [10,11]. Since successful preparation of graphene, the first two-dimensional (2D) Dirac material, it has attracted much attention because of the rare quantum Hall effect, high carrier mobility, outstanding mechanical strength, and other unique properties [12,13]. It is natural to expand the research from 2D topological semimetallic (TS) materials to three-dimensional (3D) TS compounds. Subsequently, many 3D TS carbon allotropes with novel topological nodal lines were predicted from first principles, which have significant potential applications in the higher-temperature superconductivity, superior electronic transport, and more [14–18]. By comparison, the B_{12} icosahedron is known to be a primary building block for bulk boron allotropes. However, one of the interesting issues in boron science is to find or predict the icosahedron-based 3D forms which are metallic or topologically semimetallic under ambient conditions. Such questions may be resolved by carefully tuning the ratio of B_{12} icosahedra and the interstitial atoms, and new metastable phases with fascinating properties are expected to promote the basic understanding and utility of elemental boron.

II. METHOD

To find icosahedron-based semimetallic or metallic boron structures, two steps in this paper are adopted.

(1) Structure searches were performed with 50, 52, 54, 56, 58, and 60 atoms per unit cell by using the constrained *ab initio* evolutionary algorithm USPEX [19,20]. The reason for such numbers (range) is that t-I and γ-B_{28} are included in the search, which was used to test the computational reliability.

(2) For the evolutionary search, four B_{12} icosahedra and varied single interstitial B_1 atoms (that is, $4 \times B_{12} + xB_1$, $x = 2, 4, 6, 8, 10$, and 12) were selected as building blocks, the terms of which enormously reduce the search space and improve the efficiency.

Obviously, lots of low-energy metastable structures were obtained, hence additional more accurate electronic calculations were performed to seek some particular candidates. Structure relaxations and electronic properties were conducted by using the projector-augmented wave method [21], as implemented in the VASP code [22] along with the generalized gradient approximation and the functional of Perdew, Burke, and Ernzerhof [23]. A plane-wave cutoff energy of 500 eV and uniform Γ-centered k-point grids with the resolution of $2\pi \times 0.04\,\text{Å}^{-1}$ were utilized. The convergence criteria of total energy and force were set as 10^{-6} eV and 0.01 eV/Å, respectively. Topological properties were studied through WANNIERTOOLS [24] by constructing maximally localized Wannier functions using WANNIER90 [25] and phonon dispersion curves were calculated using the PHONOPY package with the finite displacement method [26]. Elastic constants

---

[*] These coauthors contributed equally to this work.

[†] xiao.dong@nankai.edu.cn

[‡] xfzhou@nankai.edu.cn; zxf888@163.com

TABLE I. Lattice constants, density (ρ), shear modulus (G), bulk modulus (B), calculated Vickers hardness (H_v), and the total energy (E_t) of various boron allotropes at ambient pressure.

Phase	a (Å)	b (Å)	c (Å)	ρ (g/cm^3)	G (GPa)	B (GPa)	H_v (GPa)	E_t (eV/atom)
α-B_{12}	5.05	5.05	5.05	2.47	214.55	199.06	44.82	−6.704
β-B_{106}	10.10	10.16	10.16	2.33	193.20	183.31	40.57	−6.702
γ-B_{28}	5.04	5.61	6.94	2.56	237.49	209.90	50.90	−6.676
$Pnnn$-B_{52}	8.77	5.03	8.92	2.37	183.63	183.17	36.97	−6.670
α-Ga	2.94	5.32	3.27	2.81	284.43	237.99	61.55	−6.429
3D-α'	7.70	8.25	5.08	1.78	103.26	134.85	18.11	−6.357
$I2_12_12_1$-B_{60}	10.29	5.59	8.27	2.26	135.32	170.91	22.78	−6.637
$Pnma$-B_{60}	11.82	4.90	7.52	2.47	184.26	185.88	36.59	−6.596

were computed through stress-strain relations which were implemented in the CASTEP code [27]. On the basis of the Voigt-Reuss-Hill approximation [28], the bulk and shear moduli were calculated to evaluate mechanical properties.

III. RESULTS AND DISCUSSION

Indeed, t-I (probably B_{50} or B_{52}) and γ-B_{28} (with supercell form) phases together with a set of metastable structures were obtained in the search. The most low-energy metastable structures have low symmetry (e.g., $P\bar{1}$), which were not discussed further because most possess no special features. Unexpectedly, a special composition (B_{60}) with two orthorhombic phases demonstrates interesting complex structures and electronic properties. The two phases have $I2_12_12_1$ and $Pnma$ symmetries, which are designated as $I2_12_12_1$-B_{60} and $Pnma$-B_{60}, respectively. $I2_12_12_1$-B_{60} has the lowest energy within a 60-atom-unit-cell searching, which is 0.041 eV/atom lower in energy than $Pnma$-B_{60}, but 0.039 and 0.067 eV/atom higher in energy than γ-B_{28} and α-B_{12} (see Table I), implying that two orthorhombic B_{60} phases are metastable. For $I2_12_12_1$-B_{60} structure, the lattice constants are $a = 10.29$ Å, $b = 5.59$ Å, and $c = 8.27$ Å with eight nonequivalent atomic positions: B1 (0.584, 0.739, 0.362), B2 (0.332, 0.503, 0.035), B3 (0.168, 0.977, 0.960), B4 (0.190, 0.596, 0.336), B5 (0.918, 0.740, 0.463), B6 (0.189, 0.922, 0.338), B7 (0.844, 0.732, 0.658), and B8 (0.651, 0.000, 0.250). It is composed of B_{12} icosahedra and interstitial helical boron chains [Figs. 1(a) and 1(b)], the structure of which is identical to the 3D boron network of the recently predicted sodium boride, $I2_12_12_1$-Na_4B_{60} [29]. Such a new polymorph of sodium boride may coexist with the experimental $Imma$-Na_4B_{60} (or $Imm2$-Na_4B_{58}) at ambient conditions [30]. Hence one may synthesize a new boron allotrope ($I2_12_12_1$-B_{60}) by removing the Na atoms from the open framework of Na_4B_{60} because a new silicon allotrope ($Cmcm$-Si_{24}) was successfully synthesized from the precursor of Na_4Si_{24} via the thermal degassing process [31]. For $Pnma$-B_{60}, the lattice parameters are $a = 11.82$ Å, $b = 4.90$ Å, and $c = 7.52$ Å. It has ten nonequivalent B sites, which are B1 (0.520, 0.250, 0.620), B2 (0.439, 0.566, 0.564), B3 (0.111, 0.250, 0.301), B4 (0.099, 0.250, 0.691), B5 (0.249, 0.250, 0.701), B6 (0.309, 0.073, 0.520), B7 (0.690, 0.545, 0.109), B8 (0.181, 0.543, 0.623), B9 (0.266, 0.250, 0.324), and B10 (0.563, 0.428, 0.004). $Pnma$-B_{60} is also composed of B_{12} icosahedra and interstitial atoms [Figs. 1(c) and 1(d)]. It has the twisted interstitial two-atom wide ribbons with varied bond lengths from 1.72 to 1.87 Å. In contrast, $I2_12_12_1$-B_{60} has the interstitial helical chains with varied bond lengths from 1.73 to 1.76 Å. The notable difference of the interstitial bond lengths and shape between $Pnma$-B_{60} and $I2_12_12_1$-B_{60} may result in significantly different charge transfers. Hence the Bader charges of these two structures are calculated and compared for the interstitial atoms [32], which are $+0.039e$ and $+0.059e$ for $I2_12_12_1$-B_{60} compared with $-0.125e$ and $+0.056e$ for $Pnma$-B_{60}. The chemical bonds in these two phases are predominantly covalent with the partially ionic character, thus the certain degree of charge

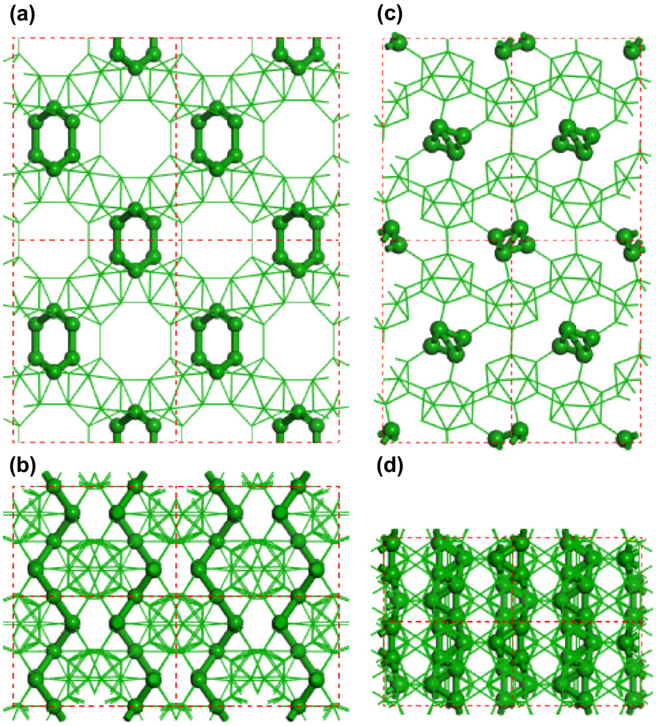

FIG. 1. (a, b) Structural projections of $I2_12_12_1$-B_{60} along [010] and [100] directions. (c, d) Structural projections of $Pnma$-B_{60} along [010] and [100] directions. For clarity, the 2 × 2 × 2 supercell is used here and the interstitial boron atoms are plotted by ball and stick form.

TABLE II. Elastic constants (in units of GPa) of $I2_12_12_1$-B_{60} and *Pnma*-B_{60}.

Phase	C_{11}	C_{22}	C_{33}	C_{44}	C_{55}	C_{66}	C_{12}	C_{13}	C_{23}
$I2_12_12_1$-B_{60}	365.28	253.4	460.27	217.11	109.20	67.21	85.42	33.53	110.68
Pnma-B_{60}	477.69	411.84	476.64	169.67	150.47	196.88	56.85	18.68	77.83

transfer makes them quasi-ionic-like elemental allotropes. More homogeneous bond lengths within the interstitial sublattice lead to uniform charge transfer, which correlates with the thermodynamic stability to some extent, in agreement with the proposed relationship between the local bonding configuration and energetic stability [33]. In this respect, that is why $I2_12_12_1$-B_{60} is more stable than *Pnma*-B_{60}.

Table I lists the lattice constants, total energies, densities, and mechanical properties of $I2_12_12_1$-B_{60}, *Pnma*-B_{60}, α-B_{12} [4], β-B_{106} [7], γ-B_{28} [5], *Pnnn*-B_{52} [8], α-Ga structure [3], and 3D-α' boron [34]. Due to the strong covalent B-B bonds, 3D boron structures are usually candidates for superhard materials. By carefully imposing the applied deformations, nine elastic constants can be determined and listed in Table II. These values satisfy the criteria of mechanical stability of orthorhombic structure given by $C_{11} > 0$, $C_{22} > 0$, $C_{33} > 0$, $C_{44} > 0$, $C_{55} > 0$, $C_{66} > 0$, $[C_{11} + C_{22} + C_{33} + 2(C_{12} + C_{13} + C_{23})] > 0$, $(C_{11} + C_{22} - 2C_{12}) > 0$, $(C_{11} + C_{33} - 2C_{13}) > 0$, $(C_{22} + C_{33} - 2C_{23}) > 0$ [35]. According to the microscopic hardness model [36,37], Vickers hardness was estimated as $H_v = 0.92k^{1.137}G^{0.708}$ and $k = G/B$, where G, B, and k are the shear modulus, bulk modulus, and Pugh modulus ratio, respectively. The Pugh modulus ratio k represents a good criterion to distinguish the brittleness and ductility of materials [37]. Table I lists the calculated hardness of 44.8 and 50.9 GPa for the α-B_{12} and γ-B_{28} phases, which are in good agreement with the experimental results ($\sim$42 GPa for α-B_{12} and 58 ± 5 GPa for γ-B_{28}) [4,38]. By applying this model to $I2_12_12_1$-B_{60} and *Pnma*-B_{60}, the calculated hardness values are 22.8 and 36.6 GPa with the corresponding k of 0.79 and 0.99, indicating that *Pnma*-B_{60} is much harder and brittler than $I2_12_12_1$-B_{60}. However, as shown in Table I, they are less hard but more ductile than α-B_{12}, β-B_{106}, or γ-B_{28} because of their relatively large empty space among the B_{12} icosahedra. Therefore, the atomic arrangements of B_{12} icosahedra and interstitial sublattices have great influence not only on the energetic stability but also on the mechanical and electronic properties.

Band structures reveal that $I2_12_12_1$-B_{60} is a conductor with large density of states (DOS) at the Fermi level (E_F), which may be tuned into a semiconductor by finite electron doping because there is a band gap above the E_F of 0.93 eV [Figs. 2(a) and 2(b)]. By comparison, as shown in Figs. 2(c) and 2(d), two valence and two conduction bands are double degenerate in pairs (without counting spin) along the high-symmetry paths *Y-T, T-Z, X-S, R-U,* and *U-X*. These valence and conduction bands (four bands) are completely degenerate along the *S-R* direction with serial quadruple degenerate contact points between S and R, while they are splitting along Γ-Y, Γ-Z, and Γ-X directions. The highest valence and lowest conduction bands mainly derived from the p orbitals of B atoms cross at a single point P (0.0 0.404 0.0) around the E_F, implying that *Pnma*-B_{60} is a potential novel TS material. Moreover, there are overlaps between the partially occupied conduction and valence bands located at the different high-symmetry points *T, S,* and *R*. From the band structure of *Pnma*-B_{60}, the densities of conduction electrons and holes can be obtained by integrating their occupations of the four bands near the E_F. The calculated electron and hole concentrations are both 1.67×10^{20} cm^{-3}, below 10^{22} cm^{-3}, which sets the upper limit for semimetals, but substantially larger than those of Dirac semimetallic Na_3Bi and Cd_3As_2 [39,40], the carrier concentrations of which are approximately 10^{17} and 10^{18} cm^{-3}, respectively. The same concentration of electrons and holes shows that *Pnma*-B_{60} is a compensated semimetal.

Depending on the degeneracy and dimensionality of the band crossings (nodes) near the E_F, topological semimetals can be classified into Dirac, Weyl, and nodal line semimetals, etc. [41–44]. Their nodes are either isolated, discrete, or forming a closed ring or periodically continuous line in momentum space, i.e., fourfold degenerate Dirac node, twofold degenerate Weyl node, and spinless twofold degenerate nodal line [44]. It has been proved that Weyl nodes generated in any crystal can only come in pairs with opposite chirality and be achieved when inversion or time-reversal symmetry is broken [44]. To distinguish the topological type of

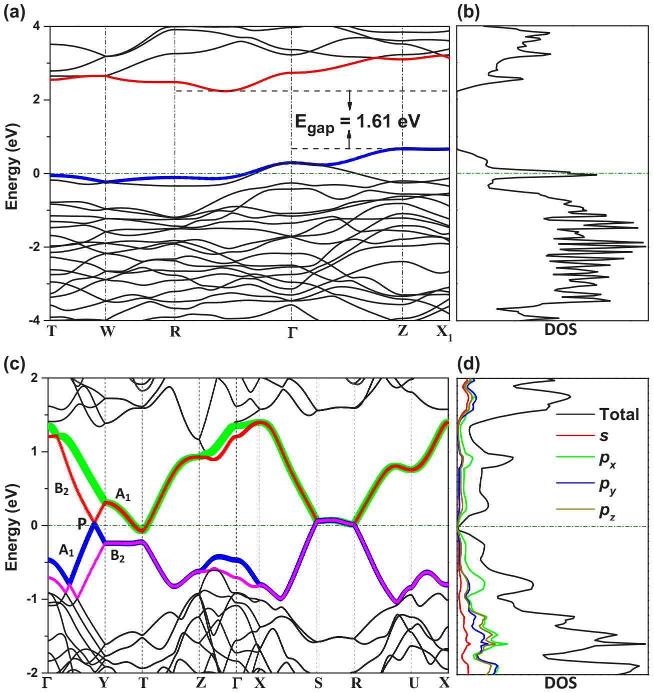

FIG. 2. Electronic structures of $I2_12_12_1$-B_{60} and *Pnma*-B_{60}. (a, b) Band structure and DOS for $I2_12_12_1$-B_{60}. (c, d) Band structure and DOS for *Pnma*-B_{60}. A_1 and B_2 indicate the irreducible representation of the two crossing bands in the vicinity of the P point.

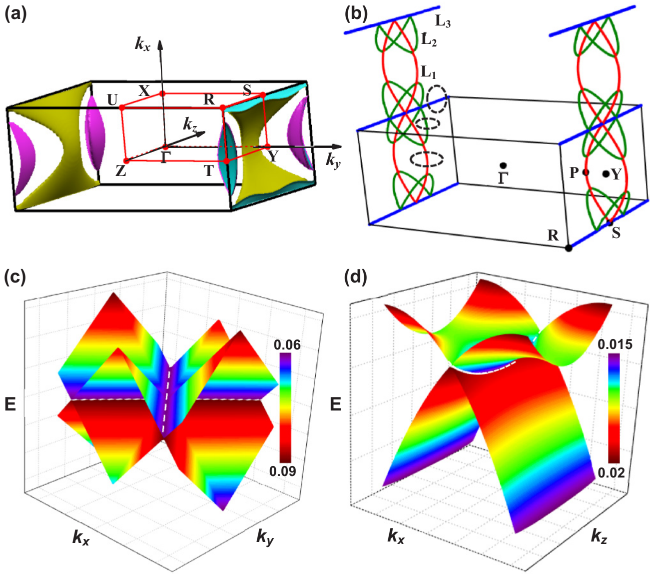

FIG. 3. (a) The calculated Fermi surface of *Pnma*-B_{60} with corresponding Brillouin zone (BZ) and the high-symmetry points are labeled accordingly. (b) The distribution of nodal lines in the extended BZ. The nodal lines L_1, L_2, and L_3 are colored in red, green, and blue, respectively. The black dashed lines represent three distinctive closed loops along which the Berry phases are calculated. (c, d) Band structures around the high-symmetry points *S* and *R* near the Fermi level. The crossing points are illustrated by white dashed lines.

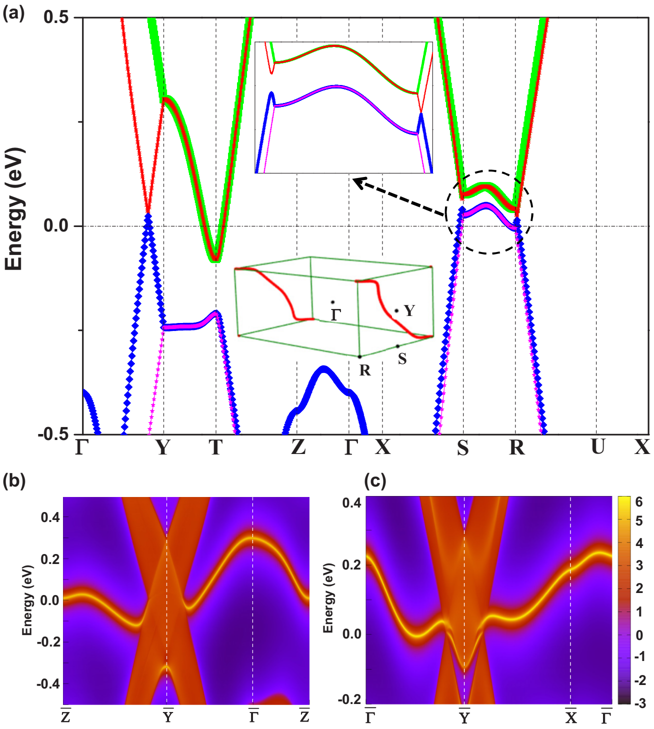

FIG. 4. (a) The band structure of *Pnma*-B_{60} under a uniaxial tensile strain (1%) along [001] direction. The upper inset shows the enlarged band structure of strained *Pnma*-B_{60} along the *X-S-R-U* paths and the lower inset reveals the redistribution of its nodal lines. (b, c) The (100) and (001) surface states of *Pnma*-B_{60}, where the color bar represents the weight of local density of states.

Pnma-B_{60}, the electronic structure analyses were presented in Fig. 3. The Fermi surface of *Pnma*-B_{60} is plotted in Fig. 3(a), showing the conduction electrons near the *T* point as well as the holes near the *P*, *S*, and *R* points. Our results also show that the crossing points of the valence and conduction bands near the E_F form complex nodal lines [Fig. 3(b)], which are labeled as L_1 (red lines), L_2 (green lines), and L_3 (blue lines), respectively. Therefore, *Pnma*-B_{60} is a compensated semimetal with coexistence of twofold and quadruple degenerate nodal lines. As shown in Fig. 2(c), the little point group along the Γ-*Y* direction is C_{2v}. It clearly shows that the crossing point *P* is protected by the symmetry with two different irreducible representations of A_1 and B_2. Therefore, the twofold degenerate nodal lines of L_1 and L_2 are formed by the inversion of the valence and conduction bands and thus protected by the coexistence of the time-reversal and inversion symmetry without taking into account the spin-orbit coupling (SOC) [15]. Nevertheless, the L_3 line, consisting of serial quadruple degenerate crossing points, forms the flatband-like dispersion along the *S-R* direction around the E_F, which is attributed to the nonsymmorphic symmetries [Figs. 3(c) and 3(d)]. To further prove this opinion, the Berry phase $\gamma = \oint_c d\vec{k}\cdot\vec{A}(\vec{k})$ is computed, where $\vec{A}(\vec{k}) = i\sum_a \langle u_{a,\vec{k}}|\nabla u_{a,\vec{k}}\rangle$ is the Berry connection of the occupied Bloch band $|u_{a,\vec{k}}\rangle$ [41,42]. For the closed loops encircling L_1, L_2, and L_3 [Fig. 3(b)], the calculations show the nontrivial π Berry phase for L_1 and L_2, and trivial zero Berry phase for L_3, indicating topological protection of L_1 and L_2, but no protection for L_3. Therefore, except for L_3, L_1 and L_2 are very robust against perturbations or impurities. The further calculations demonstrate that a uniaxial tensile strain ($\leqslant 1\%$) imposed on *Pnma*-B_{60} along the [001] direction can partially break the nonsymmorphic symmetry operators, while retaining the inversion symmetry. In this case, the twofold degenerate nodal lines persist while their distributions are changed [see the inset of Fig. 4(a)]. In contrast, the quadruple degenerate L_3 has completely disappeared, suggesting that the nonsymmorphic-symmetry-enforced degenerate L_3 is trivial and unstable. As for TS materials, one of the most important signatures is the 2D drumheadlike surface states. The semi-infinite surface states of (100) and (001) surfaces are calculated, as shown in Figs. 4(b) and 4(c), which are useful for future detection from photoelectron spectroscopy. Meanwhile, due to very weak SOC in the boron system, the SOC only opens up a tiny band gap at the crossing points, e.g., ~0.17 meV at the point of *P* and ~0.11 meV at the *S* point, which is too negligibly weak to alter its semimetallic feature. Interestingly, some boron nanobelts or nanowires are experimentally either semimetals or narrow-gap semiconductors, but their exact crystal structures are still controversial [10,11]. For *Pnma*-B_{60}, the absence of imaginary frequency in the phonon dispersion curve reveals that it is dynamically stable at ambient conditions [Figs. 5(a) and 5(b)]. Unexpectedly, the simulated electron-diffraction patterns [45] of *Pnma*-B_{60} along the [100] direction is also in satisfactory agreement with experimental results [Figs. 5(c) and 5(d)]. Comparing its semimetallic character and similar ED image with experimental data [11], *Pnma*-B_{60} may exist in the form of nanomaterials.

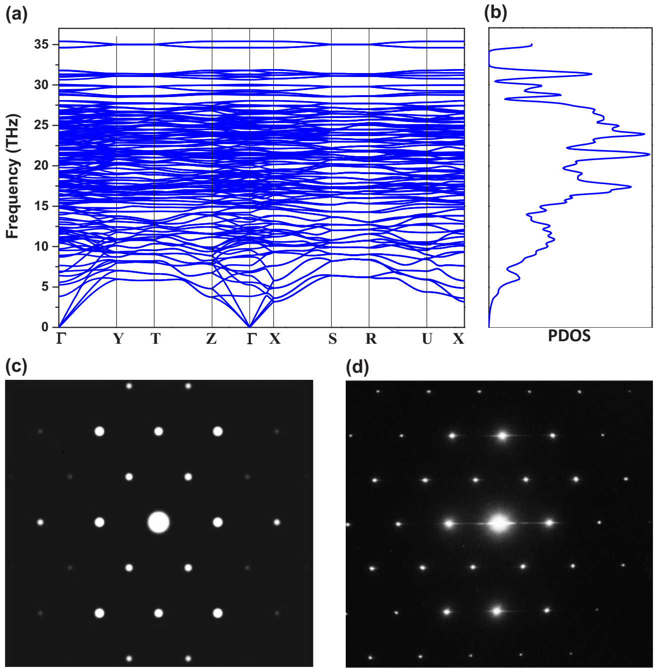

FIG. 5. (a, b) Phonon spectra and phonon density of states for *Pnma*-B_{60} at ambient condition. (c) The simulated electron diffraction (ED) pattern of *Pnma*-B_{60} along [100] direction. (d) The experimental ED pattern of certain boron nanobelts from Ref. [11].

IV. CONCLUSION

In conclusion, two orthorhombic icosahedron-based boron structures of $I2_12_12_1$-B_{60} and *Pnma*-B_{60} were predicted from the constrained *ab initio* evolutionary algorithm, which are mechanically and thermodynamically stable. The coupling between B_{12} icosahedra and interstitial sublattices is responsible for the structural and electronic diversities. Particularly, *Pnma*-B_{60} is identified to be an exotic topological nodal line semimetal with the coexistence of twofold and quadruple degeneracies, which not only enriches the phase diagram of boron but also expands its application.

ACKNOWLEDGMENTS

X.-F.Z. thanks Q.S. Wu for valuable discussions. This work was supported by the National Natural Science Foundation of China (Grants No. 11874224, No. 11674176, No. 11574133, No. 11834006, No. 21803033, and No. 11604290) and the Tianjin Science Foundation for Distinguished Young Scholars (Grant No. 17JCJQJC44400). X.-F.Z. thanks the National Key Research and Development Program of China (Grant No. YS2018YFA070119). X.D. and X.-F.Z. thank the computing resources of Tianhe II and the support of Chinese National Supercomputer Center in Guangzhou.

---

[1] B. Albert and H. Hillebrecht, Angew. Chem. Int. Ed. **48**, 8640 (2009).

[2] M. I. Eremets, V. V. Struzhkin, H.-k. Mao, and R. J. Hemley, Science **293**, 272 (2001).

[3] U. Häussermann, S. I. Simak, R. Ahuja, and B. Johansson, Phys. Rev. Lett. **90**, 065701 (2003).

[4] J. He, E. Wu, H. Wang, R. Liu, and Y. J. Tian, Phys. Rev. Lett. **94**, 015504 (2005).

[5] A. R. Oganov, J. H. Chen, C. Gatti, Y. Z. Ma, Y. M. Ma, C. W. Glass, Z. X. Liu, T. Yu, O. O. Kurakevych, and V. L. Solozhenko, Nature (London) **457**, 863 (2009).

[6] G. Parakhonskiy, N. Dubrovinskaia, E. Bykova, R. Wirth, and L. Dubrovinsky, High Press. Res. **33**, 673 (2013).

[7] Q. An, K. M. Reddy, K. Y. Xie, K. J. Hemker, and W. A. Goddard III, Phys. Rev. Lett. **117**, 085501 (2016); **118**, 159902(E) (2017).

[8] E. A. Ekimov, Y. B. Lebed, N. Uemura, K. Shirai, T. Shatalova, and V. Sirotinkin, J. Mater. Res. **31**, 2773 (2016).

[9] K. Shirai, Jpn. J. Appl. Phys. **56**, 05FA06 (2017).

[10] C. J. Otten, O. R. Lourie, M. F. Yu, J. M. Cowley, M. J. Dyer, R. S. Ruoff, and W. E. Buhro, J. Am. Chem. Soc. **124**, 4564 (2002).

[11] Y. Sato, M. Terauchi, K. Kirihara, T. Sasaki, K. Kawaguchi, N. Koshizaki, and K. Kimura, J. Phys. Conf. Ser. **176**, 012029 (2009).

[12] K. S. Novoselov, A. K. Geim, S. V. Morozov, D. Jiang, Y. Zhang, S. V. Dubonos, I. V. Grigorieva, and A. A. Firsov, Science **306**, 666 (2004).

[13] A. H. Castro Neto, F. Guinea, N. M. R. Peres, K. S. Novoselov, and A. K. Geim, Rev. Mod. Phys. **81**, 109 (2009).

[14] Y. Chen, Y. Xie, S. A. Yang, H. Pan, F. Zhang, M. L. Cohen, and S. Zhang, Nano Lett. **15**, 6974 (2015).

[15] H. Weng, Y. Liang, Q. Xu, R. Yu, Z. Fang, X. Dai, and Y. Kawazoe, Phys. Rev. B **92**, 045108 (2015).

[16] K. Mullen, B. Uchoa, and D. T. Glatzhofer, Phys. Rev. Lett. **115**, 026403 (2015).

[17] J.-T. Wang, H. Weng, S. M. Nie, Z. Fang, Y. Kawazoe, and C. F. Chen, Phys. Rev. Lett. **116**, 195501 (2016).

[18] J.-T. Wang, S. Nie, H. Weng, Y. Kawazoe, and C. Chen, Phys. Rev. Lett. **120**, 026402 (2018).

[19] A. R. Oganov and C. W. Glass, J. Chem. Phys. **124**, 244704 (2006).

[20] C. W. Glass, A. R. Oganov, and N. Hansen, Comput. Phys. Commun. **175**, 713 (2006).

[21] P. E. Blöchl, Phys. Rev. B **50**, 17953 (1994).

[22] G. Kresse and J. Furthmüller, Phys. Rev. B **54**, 11169 (1996); Comput. Mater. Sci. **6**, 15 (1996).

[23] J. P. Perdew, K. Burke, and M. Ernzerhof, Phys. Rev. Lett. **77**, 3865 (1996).

[24] Q. S. Wu, S. N. Zhang, H.-F. Song, M. Troyera, and A. A. Soluyanov, Comput. Phys. Commun. **224**, 405 (2018).

[25] A. A. Mostofi, J. R. Yates, Y.-S. Lee, I. Souza, D. Vanderbilt, and N. Marzari, Comput. Phys. Commun. **178**, 685 (2008).

[26] A. Togo and I. Tanaka, Scr. Mater. **108**, 1 (2015).

[27] S. J. Clark, M. D. Segall, C. J. Pickard, P. J. Hasnip, M. I. J. Probert, K. Refson, and M. C. Payne, Z. Kristallogr. **220**, 567 (2005).

[28] R. Hill, Proc. Phys. Soc. A London **65**, 349 (1952).

[29] X.-L. He, X. Dong, Q. S. Wu, Z. Zhao, Q. Zhu, A. R. Oganov, Y. Tian, D. Yu, X.-F. Zhou, and H.-T. Wang, Phys. Rev. B **97**, 100102(R) (2018).

[30] B. Albert, K. Hofmann, C. Fild, H. Eckert, M. Schleifer, and R. Grurhn, Chem. Eur. J. **6**, 2531 (2000).

[31] D. Y. Kim, S. Stefanoski, O. O. Kurakevych, and T. A. Strobel, Nat. Mater. **14**, 169 (2015).

[32] W. Tang, E. Sanville, and G. Henkelman, J. Phys. Condens. Matter **21**, 084204 (2009).

[33] X.-F. Zhou, A. R. Oganov, G.-R. Qian, and Q. Zhu, Phys. Rev. Lett. **109**, 245503 (2012).

[34] Y. Gao, Y. Xie, Y. Chen, J. Gu, and Z. Chen, Phys. Chem. Chem. Phys. **20**, 23500 (2018).

[35] Z.-J. Wu, E.-J. Zhao, H.-P. Xiang, X.-F. Hao, X.-J. Liu, and J. Meng, Phys. Rev. B **76**, 054115 (2007).

[36] Y. Tian, B. Xu, and Z. Zhao, Int. J. Refract. Met. Hard Mater. **33**, 93 (2012).

[37] X.-Q. Chen, H. Niu, D. Li, and Y. Li, Intermetallics **19**, 1275 (2011).

[38] E. Yu. Zarechnaya, L. Dubrovinsky, N. Dubrovinskaia, Y. Filinchuk, D. Chernyshov, V. Dmitriev, N. Miyajima, A. El Goresy, H. F. Braun, S. Van Smaalen, I. Kantor, A. Kantor, V. Prakapenka, M. Hanfland, A. S. Mikhaylushkin, I. A. Abrikosov, and S. I. Simak, Phys. Rev. Lett. **102**, 185501 (2009).

[39] J. Xiong, S. K. Kushwaha, T. Liang, J. W. Krizan, M. Hirschberger, W. Wang, R. J. Cava, and N. P. Ong, Science **350**, 413 (2015).

[40] T. Liang, Q. Gibson, M. N. Ali, M. Liu, R. J. Cava, and N. P. Ong, Nat. Mater. **14**, 280 (2015).

[41] X. Wan, A. M. Turner, A. Vishwanath, and S. Y. Savrasov, Phys. Rev. B **83**, 205101 (2011).

[42] A. A. Burkov, M. D. Hook, and L. Balents, Phys. Rev. B **84**, 235126 (2011).

[43] S. M. Young, S. Zaheer, J. C. Y. Teo, C. L. Kane, E. J. Mele, and A. M. Rappe, Phys. Rev. Lett. **108**, 140405 (2012).

[44] H. Weng, X. Dai, and Z. Fang, J. Phys.: Condens. Matter **28**, 303001 (2016).

[45] http://www.crystalmaker.com/.